iScience

CellPress

Article

Thermoelectric Flexible Silver Selenide Films: Compositional and Length Optimization

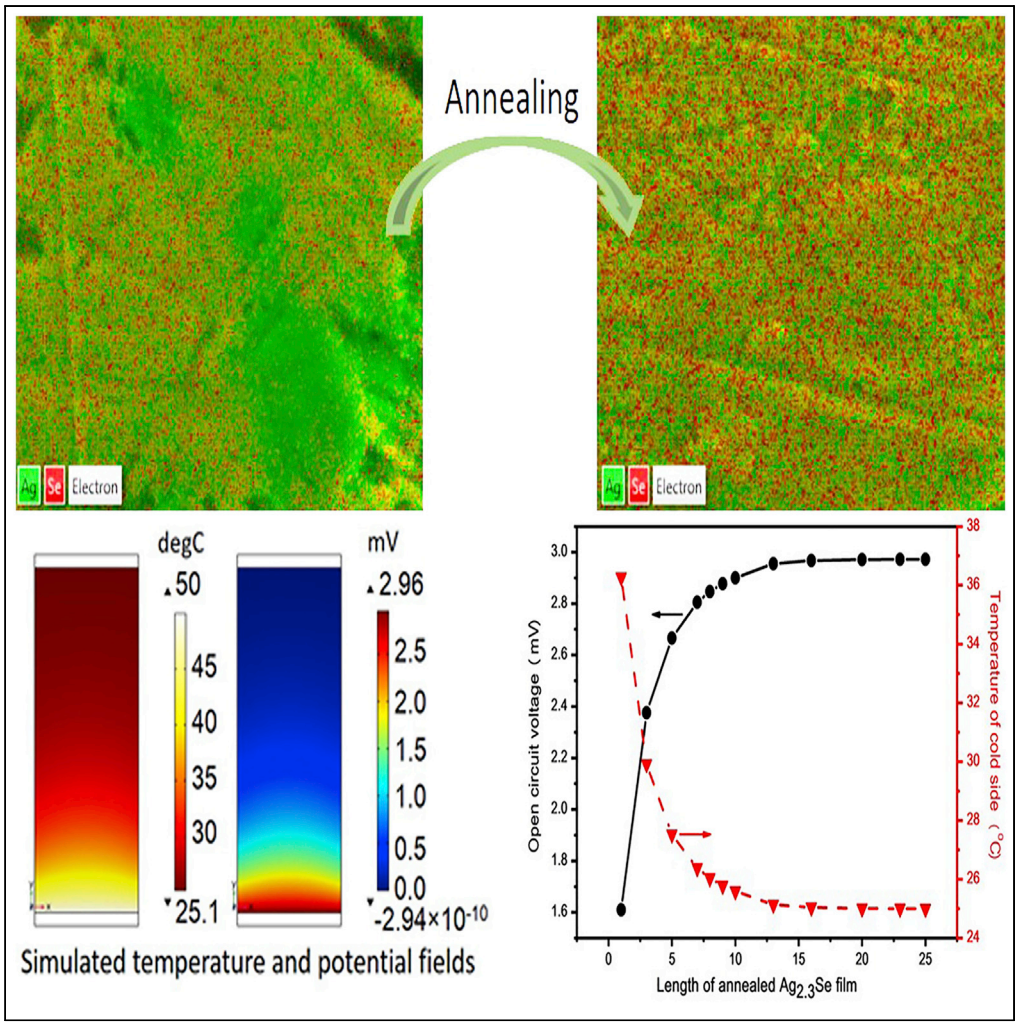

Jie Gao, Lei Miao, Huajun Lai, ..., Xiaoyang Wang, Kunihito Koumoto, Huanfu Cai

miaolei@guet.edu.cn

HIGHLIGHTS

A remarkably improved power factor is achieved by annealing treatment

Optimal length of Ag-rich Ag_2Se film is obtained via a numerical simulation

A high output power density at temperature difference of 25 K is realized

Gao et al., iScience *23*, 100753 January 24, 2020
https://doi.org/10.1016/j.isci.2019.100753

iScience

CellPress

Article

Thermoelectric Flexible Silver Selenide Films: Compositional and Length Optimization

Jie Gao,[1] Lei Miao,[1,7,*] Huajun Lai,[1] Sijing Zhu,[1] Ying Peng,[1,2] Xiaoyang Wang,[1,3] Kunihito Koumoto,[4,5] and Huanfu Cai[6]

SUMMARY

Silver selenide is considered as a promising room temperature thermoelectric material due to its excellent performance and high abundance. However, the silver selenide-based flexible film is still behind in thermoelectric performance compared with its bulk counterpart. In this work, the composition of paper-supported silver selenide film was successfully modulated through changing reactant ratio and annealing treatment. In consequence, the power factor value of 2450.9 $\pm$ 364.4 $\mu W/(mK^2)$ at 303 K, which is close to that of state-of-the-art bulk Ag_2Se has been achieved. Moreover, a thermoelectric device was fabricated after optimizing the length of annealed silver selenide film via numerical simulation. At temperature difference of 25 K, the maximum power density of this device reaches 5.80 W/m^2, which is superior to that of previous film thermoelectric devices. Theoretically and experimentally, this work provides an effective way to achieve silver-selenide-based flexible thermoelectric film and device with high performance.

INTRODUCTION

Wearable electronic devices is expected to play an important role in addressing the issue of an individual's timely healthcare, real-time safety monitoring, and life improvement (Gao et al., 2017a; Hu et al., 2019). Indisputably, for the wearable electronic devices, being continuously operated, mechanically flexible, biocompatible, and easy to maintain is of critical importance. Nonetheless, most of the available wearable electronic devices are still powered by rigid batteries that require frequent charging or replacement, which leads to a lot of problems, such as poor flexibility, inconvenience, and environmental pollution. As a result, the self-powered flexible electronic devices that can work constantly without an external power supply are extremely in demand (Yang et al., 2018; Lou et al., 2017).

To date, in general, based on piezoelectric or triboelectric effect, photovoltaic effect, and thermoelectric effect, the mechanical energy, solar energy, and thermal energy can be accordingly converted into electrical energy for wearable electronic devices (Jeon et al., 2016; Zi and Wang, 2017; Kim et al., 2016). Compared with the piezoelectric, triboelectric, and photovoltaic energy harvesters, the flexible thermoelectric generators can directly generate electricity by utilizing the temperature difference between the skin and the ambient environment all-weather, regardless of the motion state of human body. Therefore, in recent ten years, flexible thermoelectric materials and generators have drawn greatly increasing attention (Du et al., 2018), and a variety of conductive polymers (Kroon et al., 2016), carbon materials (Gao et al., 2016), nano-sized inorganic semiconductors (Dun et al., 2015), and metals (Chen et al., 2017) have been applied to fabricate flexible thermoelectric films. So far, in spite of their relatively poor flexibility, the nano-sized inorganic semiconductors are superior to their counterparts because of their excellent thermoelectric performance.

Currently, the cost-effective and abundant metal sulfides and metal selenides are hot topics in the research of thermoelectric materials applied over from room temperature to moderate temperature (Ge et al., 2016; Zhao et al., 2014; Li et al., 2016), and due to its high power factor and low thermal conductivity at room temperature, the silver selenide is considered to be a promising substitute for commercial Bi_2Te_3-based alloy (Ferhat and Nagao, 2000). Day et al. predicted that by reducing carrier concentration to 1.6×10^{18} cm^{-3}, a *ZT* value higher than 1 from 300 K to 600 K can be realized in $Ag_{2+x}Se$ (Day et al., 2013), and previous study reveals that the carrier concentration can be regulated by changing molar ratio of Ag/Se in the silver selenide samples (Lee et al., 2007; Mi et al., 2014; Perez-Taborda et al., 2018). For instance, Lee et al. investigated a series of samples with Ag/Se varying from 1.73 to 2.33, and it is found that the excess silver atoms promote the carrier concentration and diminish the Hall carrier mobility (Lee et al., 2007). Perez-Taborda et al. demonstrated that the *PF*

[1]Guangxi Key Laboratory of Information Material, Guangxi Collaborative Innovation Center of Structure and Property for New Energy and Materials, School of Materials Science and Engineering, Guilin University of Electronic Technology, Guilin 541004, China

[2]Department of Materials Physics, Graduate School of Engineering, Nagoya University, Furo-cho, Chikusa-ku, Nagoya 464-8603, Japan

[3]Department of Chemical Systems Engineering, Graduate School of Engineering, Nagoya University, Furo-cho, Chikusa-ku, Nagoya 464-8603, Japan

[4]Nagoya Industrial Science Research Institute, Nagoya 464-0819, Japan

[5]Center of Nanotechnology, King Abdulaziz University, Jeddah 21589, Saudi Arabia

[6]School of Internet Finance and Information Engineering, Guangdong University of Finance, Guangzhou 510520, China

[7]Lead Contact

*Correspondence: miaolei@guet.edu.cn

https://doi.org/10.1016/j.isci.2019.100753

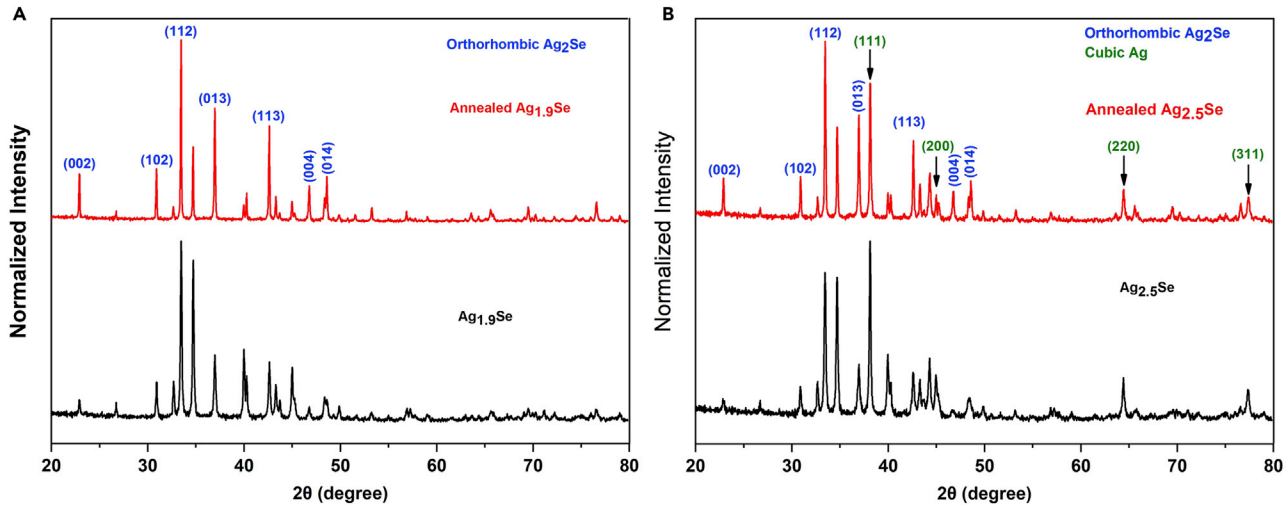

Figure 1. Phase Characterization of Silver Selenide Film before and after Being Annealed

XRD patterns of $Ag_{1.9}Se$ film (A) and $Ag_{2.5}Se$ film (B) before and after being annealed. This figure is related to Figure S1 and Table S1.

value of accurately controlled stoichiometric Ag_2Se thin film on glass substrate reached up to 2440 ± 192 μW m^{-1} K^{-2} at room temperature (Perez-Taborda et al., 2018). Besides the non-flexible silver selenide materials, the flexible silver selenide film with outstanding performance has also been reported very recently. Cai's group published two articles about nylon-membrane-supported Ag_2Se-nanowire-based flexible films in succession (Ding et al., 2019; Lu et al., 2019), and an outstanding *PF* value of 2231.5 $\mu Wm^{-1}K^{-2}$ at 300 K for flexible thermoelectric film was realized in CuAg4Se3 composite films.

Despite the fact that remarkable progress has been made in silver-selenide-based flexible thermoelectric film, there is still room for further improvement of their power factor. On the other hand, researches on bulk thermoelectric generators show that for the thermoelectric leg with a certain cross-sectional area, its output power increases first and then decreases with increasing length of thermoelectric leg, thus, the maximum output power is obtained in thermoelectric leg with ideal length (Ferreira-Teixeira and Pereira, 2018; Zhang et al., 2018). However, most of the studies on flexible thermoelectric films are confined to improving the power factor of materials, while ignoring the optimization of leg geometry configuration in flexible thermoelectric generators, which greatly determines the output voltage and output power density (Madan et al., 2015). In this work, by simply varying the molar ratio of $AgNO_3$ to Se from 1.9 to 2.5, the silver selenide NPs with different content of Ag were synthesized via a solvothermal reaction. Subsequently, the flexible paper-supported silver selenide NPs films were fabricated by our previously reported cold-press method (Gao et al., 2017b). The highest *PF* value of 1674.1 μW/(mK^2) at 303 K was achieved in the sample $Ag_{2.3}Se$ film ($AgNO_3$/Se = 2.3). Then the composition of these films was further modulated by annealing the films in Ar/H_2 atmosphere at 250°C for 2 h. According to the XRD spectra and EDX mapping images, after being annealed, for all samples, the crystallinity of Ag_2Se phase was enhanced, the molar ratio of Ag/Se was greatly reduced, and the distribution of Ag in the film was more uniform. As a result, all of the annealed films showed significantly improved *PF* values, and the highest *PF* value of the annealed $Ag_{2.3}Se$ film reached up to 2450.9 ± 364.4 μW/(mK^2) at 303 K, which is close to that of state-of-the-art bulk silver selenide materials. Moreover, according to the results of numerical simulation, the optimal length of single annealed $Ag_{2.3}Se$ film (the width is 5 mm) is calculated to be 13 mm. By series-connecting four pieces of annealed $Ag_{2.3}Se$ films with silver paste, a paper-supported thermoelectric module was fabricated. At temperature difference of about 25 K, the maximum output power density reaches up to 5.80 W/m^2, which is superior to other film thermoelectric devices.

RESULTS AND DISCUSSION

Phase and Morphology of Silver Selenide Nanoparticles and Films

The XRD patterns of $Ag_{1.9}Se$ and $Ag_{2.5}Se$ films before and after being annealed are compared in Figure 1. As shown in Figure 1A, all peaks in XRD pattern of $Ag_{1.9}Se$ film can be indexed to the orthorhombic Ag_2Se, and in Figure 1B, the XRD patterns of $Ag_{2.5}Se$ films show characteristic peaks of orthorhombic Ag_2Se and

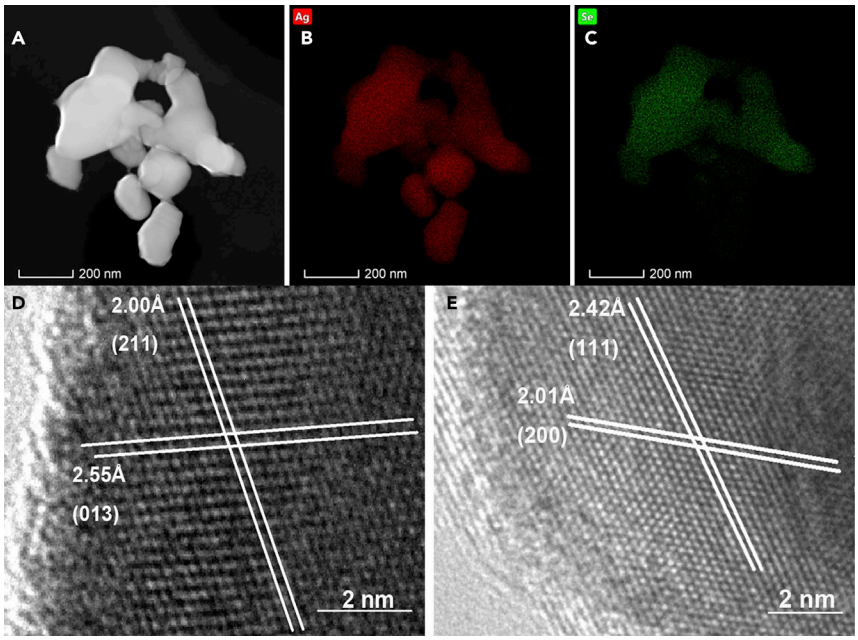

Figure 2. Composition and Crystal Lattice of $Ag_{2.5}Se$ Particles

TEM image (A), TEM-EDS maps (B and C) and HRTEM images (D and E) of $Ag_{2.5}Se$ particles. (D) and (E) reveal the HRTEM images of Ag_2Se phase and Ag phase in $Ag_{2.5}Se$ particles, respectively. In (A), (B) and (C), the scale bar is 200 nm, and in (D) and (E), the scale bar is 2 nm.

cubic Ag. In addition, in the XRD spectra of annealed films, the relative intensity of peaks corresponding to (002), (102), (112), (013), (113), (004), and (014) planes of Ag_2Se are obviously enhanced, whereas the relative intensity of peaks indexed to cubic Ag are weakened, which indicates that the content of Ag has been reduced in the annealed $Ag_{2.5}Se$ film. The XRD spectra of other films are displayed in Figure S1, and they exhibit the same change as that of $Ag_{2.5}Se$ films. On the other hand, as shown in Table S1, for all annealed silver selenide films, the full width at half maximum (FWHM) values of dominant peak [(112) plane] are reduced, implying that the annealing treatment leads to the enhanced crystallinity of Ag_2Se phase.

In Figure 2A, the TEM image clearly shows particles with different sizes and shapes. Further, the TEM-EDS maps in Figures 2B and 2C suggest that the small-sized near-spherical particles are Ag nanoparticles and the large-sized irregular particles are Ag_2Se nanoparticles. Figure 2D displays the HRTEM image of Ag_2Se nanoparticle, and the interplanar distances of 2.55 Å and 2.00 Å correspond to the lattice spaces of (013) and (211) planes. The HRTEM image of Ag nanoparticles in Figure 2E shows the (200) and (111) planes with interplanar distances of 2.01 Å and 2.42 Å.

Figure 3 reveals the representative morphology of silver selenide particles and films, and more SEM images of silver selenide particles and films are presented in Figure S2. As shown in Figures 3A and 3B, the large-sized (1–2 μm) and small-sized (100–200 nm) particles with different shapes can be found in both of the two samples. Meanwhile, with increasing ratio of Ag/Se, more particles with small size are observed in the images, indicating that more Ag are contained in the sample. Figures 3C and 3D show the relatively smooth surface of paper-supported films, suggesting that the morphology of particles and the boundaries among particles have almost been destroyed due to the compression, and the similar result has been reported in our previous work (Gao et al., 2017b). As exhibited in Figures 3E and 3F, no obvious change can be found in the annealed films, which indicates that the annealing treatment has little impact on the morphology of silver selenide films. The cross-sectional SEM image of a piece of annealed $Ag_{2.5}Se$ film is shown in Figure S3, and it can be deduced from this figure that the thickness of silver selenide films is about 10 μm.

Compositional Modulation and Regulation of Carrier Transport Characteristics

The SEM-EDS maps in Figure 4 illustrate the varied composition of silver selenide films before and after being annealed. As shown in Figure 4A, although some tiny Ag aggregations can be observed in limited

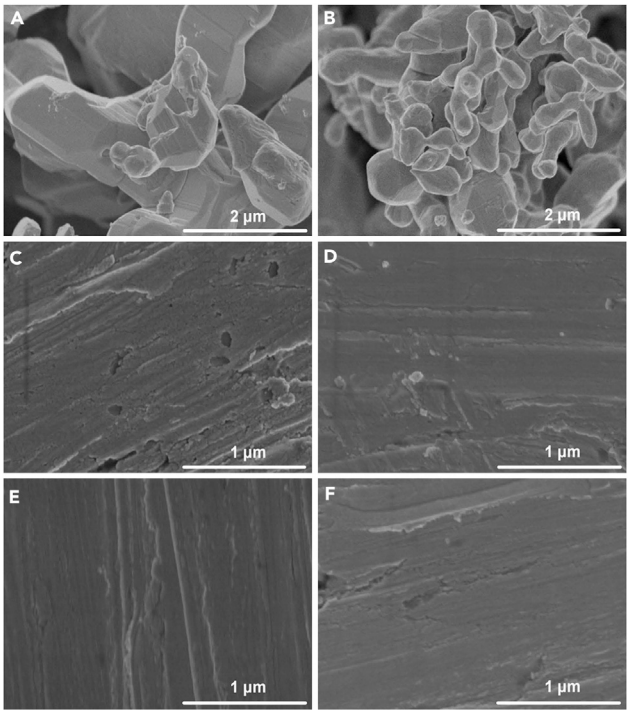

Figure 3. Morphology of Silver Selenide Particles and Films

The representative SEM images of silver selenide particles and paper-supported films. $Ag_{1.9}Se$ and $Ag_{2.5}Se$ particles (A and B), $Ag_{1.9}Se$ and $Ag_{2.5}Se$ films (C and D), and annealed $Ag_{1.9}Se$ and $Ag_{2.5}Se$ films (E and F). The scale bar is 1 μm and this figure is related to Figures S2 and S3.

regions, the Ag and Se elements are almost uniformly distributed in the $Ag_{1.9}Se$ film. On the contrary, Figure 4B clearly shows that Ag aggregation with size of micrometers can be found in the $Ag_{2.5}Se$ film. Then in the SEM-EDS maps of annealed films, the signal of Ag element is obviously reduced and the area of Ag aggregations in annealed $Ag_{2.5}Se$ films is greatly shrunk. These results can also be observed in SEM-EDS maps of other silver selenide films (Figure S4 in Supplemental Information). Despite the EDS maps can only provide semi-quantitative results, based on the SEM-EDS maps, the molar ratios of Ag/Se in silver selenide films before and after being annealed are calculated and listed in Table 1. This table reveals that all samples are Ag-rich silver selenide films, and the annealing treatment indeed leads to the decreased concentrations of Ag element in films, especially in the film containing more Ag element, such as $Ag_{2.5}Se$ film.

All in all, it can be concluded from XRD patterns and SEM-EDS maps that due to the annealing treatment, the compositions of silver selenide films have been modulated and the crystallinity of Ag_2Se phase in the films has been improved. As a result, the carrier transport characteristics of silver selenide films have also been regulated. As shown in Figure 5, on the whole, the carrier concentrations of all films are diminished because of the annealing treatment, in particular those of the films with high content of Ag ($Ag_{2.1}Se$ to $Ag_{2.5}Se$), and this result is in consistence with the reduction of Ag in the films, which has been verified by SEM-EDS maps. As shown in SEM-EDS maps, for the film with less Ag ($Ag_{1.9}Se$ film), the annealing treatment has less impact on the content of Ag in the film, whereas for the film with more Ag, for example, $Ag_{2.5}Se$ film, the content of Ag in the film is greatly reduced by annealing treatment. Accordingly, the carrier concentration of film with less Ag is slightly changed, whereas that of film with more Ag is obviously decreased due to the annealing treatment. Moreover, the shrinkage of Ag aggregation regions possibly increases the amount of nano-sized interfaces between Ag and Ag_2Se in the film, whereas the energy filtering effect on the nano-sized interfaces also leads to the reduction of carrier concentration (Lu et al., 2019). On the other hand, after being annealed, all films show almost doubled carrier mobility, and this increased carrier mobility results from two reasons. First, the enhanced crystallinity of Ag_2Se phase in the annealed films is benefit for increasing carrier mobility. Second, the decreased carrier concentration

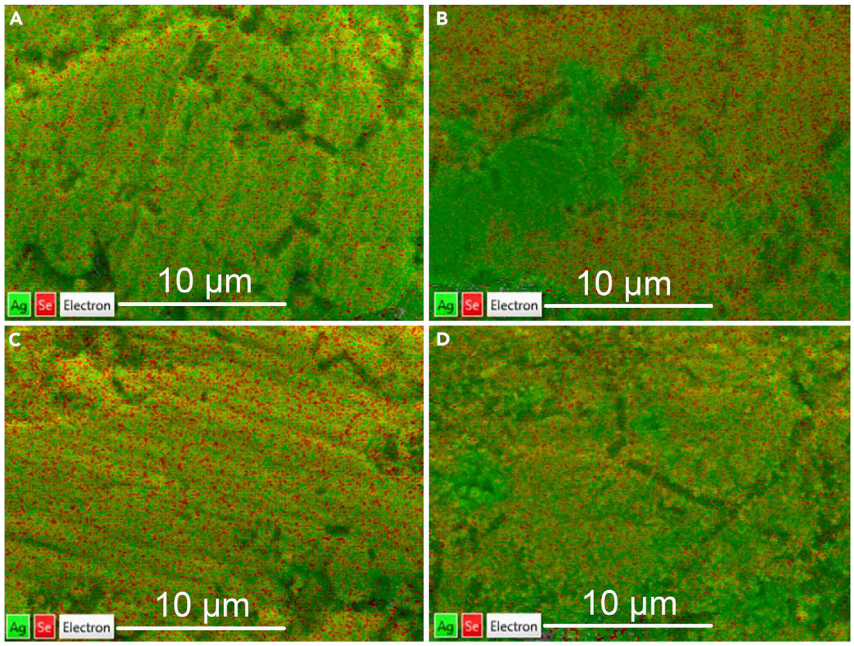

Figure 4. Elemental Distribution in Silver Selenide Films before and after Being Annealed

The representative SEM-EDS maps of silver selenide films before and after being annealed. $Ag_{1.9}Se$ film (A), $Ag_{2.5}Se$ film (B), annealed $Ag_{1.9}Se$ film (C), and $Ag_{2.5}Se$ film (D). The scale bar is 10 μm and this figure is related to Figure S4.

in annealed films leads to weaker scattering among carriers, which also contributes to the improvement of carrier mobility.

Thermoelectric Properties of Silver Selenide Films

Figure 6 displays the thermoelectric properties at 303 K of silver selenide films before and after being annealed, and the trend of electrical resistivity in Figure 6A is in accordance with that of product of n and μ. The resistivity decreases with increasing molar ratio of $AgNO_3$/Se and after being annealed, the $Ag_{1.9}Se$ and $Ag_{2.0}Se$ films show the markedly reduced resistivity, whereas other films show the slightly increased resistivity. Before being annealed, the $Ag_{2.5}Se$ film possesses the lowest resistivity of $(0.5 \pm 0.025) \times 10^{-5}$ Ω/m and this value turns to be $(0.52 \pm 0.026) \times 10^{-5}$ Ω/m for the annealed $Ag_{2.5}Se$ film. The Seebeck coefficients in Figure 6B show a similar changing tendency to that of electrical resistivity. As to the annealed films, the Seebeck coefficients of $Ag_{1.9}Se$ and $Ag_{2.0}Se$ films are reduced, whereas those of other films are raised. Before being annealed, the $Ag_{1.9}Se$ film shows the largest Seebeck coefficient of -140.1 ± 9.8 μV/K, which is very close to the value reported in previous work (Ding et al., 2019). For comparison, the Seebeck coefficients of films prepared with smaller ratios of $AgNO_3$/Se (from 1.8 to 1.5) are measured and displayed in Figure S5. According to Figure S5, it can be concluded that the further reduction of $AgNO_3$ is not helpful to improve the Seebeck coefficient of silver selenide film. In Figure 6C, the power factor increases and then decreases with the increasing molar ratio of $AgNO_3$/Se, and all films show the enhanced power factors after being annealed. The highest power factor of films before being annealed is 1674.1 ± 248.9 μW/(mK^2),

	$Ag_{1.9}Se$ Film	Annealed $Ag_{1.9}Se$ Film	$Ag_{2.1}Se$ Film	Annealed $Ag_{2.1}Se$ Film	$Ag_{2.3}Se$ Film	Annealed $Ag_{2.3}Se$ Film	$Ag_{2.5}Se$ Film	Annealed $Ag_{2.5}Se$ Film
Ag	69.92	68.69	72.94	71.66	75.96	73.76	78.13	74.06
Se	30.08	31.31	27.06	28.34	24.04	26.24	21.87	25.94
Ag/Se	2.32	2.19	2.70	2.53	3.16	2.81	3.57	2.85

Table 1. The Molar Ratios of Ag/Se in Silver Selenide Films before and after Being Annealed

This table is related to Figure S4.

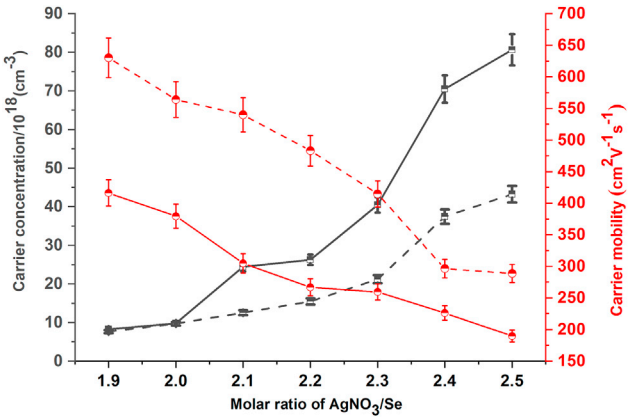

Figure 5. Carrier Transport Characteristics of Silver Selenide Films before and after Being Annealed

The carrier concentration (▬) and mobility (◓) of silver selenide films before (solid line) and after (dash line) being annealed, and both of the errors of carrier concentration and mobility are ±5%.

which is realized in the $Ag_{2.3}Se$ film, and this value is remarkably improved to be 2450.9 ± 364.4 μW/(mK^2) for the annealed $Ag_{2.3}Se$ film.

The thermoelectric properties of annealed silver selenide films at different temperatures are shown in Figure 7. In Figure 7A, the resistivity significantly decreases and then slightly increases with the temperature for measurement increasing from 30°C to 210°C, and this trend is attributed to the phase transition of Ag_2Se. The phase transition temperature of Ag_2Se is about 133°C (Xiao et al., 2012), and Ag_2Se with orthorhombic structure (β-Ag_2Se) is a semiconductor, so the resistivity of annealed films decreases with increasing temperature when the temperature is below 133°C. Then once the temperature for measurement is above 150°C, the Ag_2Se has been transformed from orthorhombic structure to cubic structure (α-Ag_2Se), which shows conductive character of metal. Similarly, as exhibited in Figure 7B, with the temperature increasing from 30°C to 150°C, the absolute value of Seebeck coefficient remarkably drops from over 100 μV/K to around 30 μV/K; when the temperature continues to rise from 150°C to 210°C, it turns to ascend slightly. This variation tendency of Seebeck coefficient also results from the phase transition of Ag_2Se. Because of the variation of resistivity and Seebeck coefficient, all annealed films display the highest power factors at 90°C in Figure 7C, and the maximum of power factor is realized in the annealed $Ag_{2.3}Se$ film, reaching up to 2610.9 ± 388.0 μW/(mK^2). The power factor at around 300 K of annealed $Ag_{2.3}Se$ film in this work is compared with those of representative bulk silver selenide materials, Ag_2Se-based flexible films, and Bi-TeSe film (Table 2); it can be concluded from this table that among the Ag_2Se-based flexible film, the power factor of annealed $Ag_{2.3}Se$ film in this work is closest to that of Ag_2Se-based bulk materials.

It is very difficult to obtain the accurate in-plane thermal conductivity of a substrate-supported thin film due to the following reasons. First, the thickness of sample for the laser flash diffusivity apparatus is usually 1–2 mm, which is much larger than that of flexible film, thus it is almost impossible to obtain the cross-plane thermal diffusivity of thin film by a general commercial laser flash diffusivity apparatus. Second, for the film with high electrical conductivity (>500 S/cm), the anisotropy in thermal conductivity can be as large as 1:0.3 (in-plane: cross-plane) (Liu et al., 2015). Third, the substrate contribution must be removed (Bahk et al., 2015), and if the electrical conductivity and the thermal conductivity were measured from two different sets of samples, a large uncertainty in the ZT value would be resulted in (Weathers et al., 2015). As a reference, the thermal diffusivity and specific heat capacity of annealed $Ag_{2.3}Se$ pellet has been measured and displayed in Figure S6, and the thermal conductivity of annealed $Ag_{2.3}Se$ pellet is calculated to be 0.635 W/(mK) at 303 K. However, we find that the paper substrate might also play a role in determining the composition of silver selenide film due to the possible reaction between paper substrate and the Ag_2Se or Ag particles in the film at the temperature for annealing treatment (250°C), and there is no paper substrate attached with the $Ag_{2.3}Se$ pellet during the annealing treatment, thus the composition and electrical and thermal properties of annealed $Ag_{2.3}Se$ film and $Ag_{2.3}Se$ pellet are likely to be different. Because the specific influence of paper substrate on silver selenide during the process of annealing treatment is remained to be investigated in our following work, it is reasonable to use the theoretic thermal conductivity of

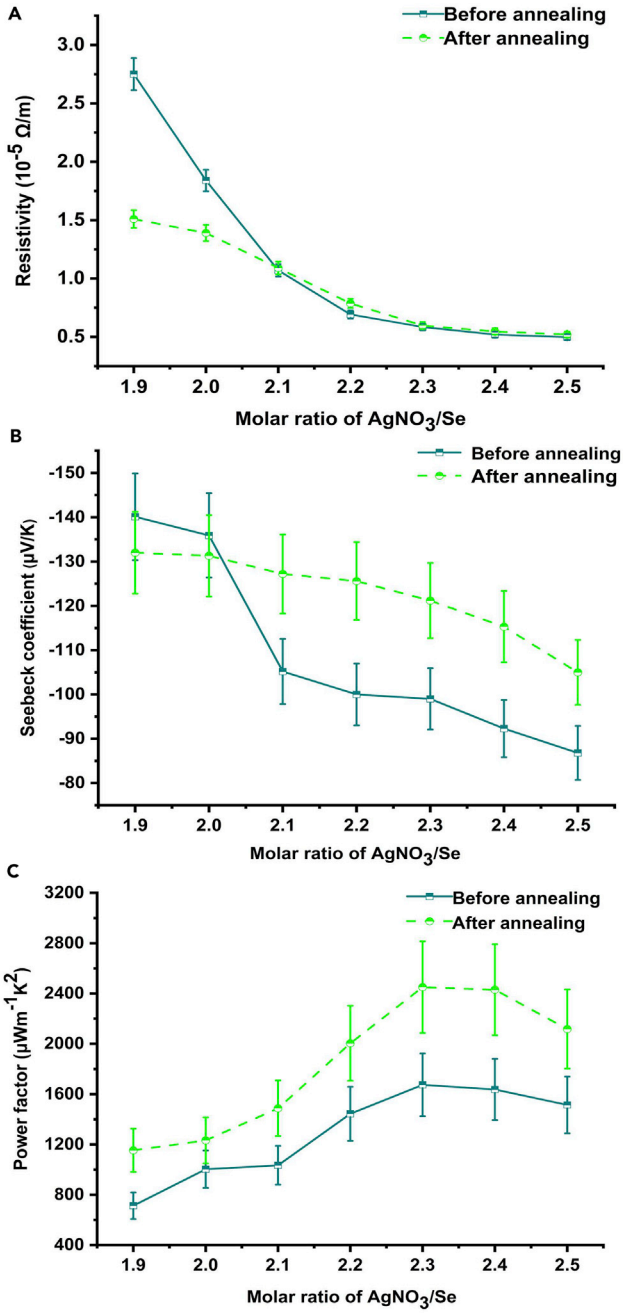

Figure 6. The Thermoelectric Properties of Silver Selenide Films before and after Being Annealed

The electrical resistivity (A), Seebeck coefficient (B), and power factor (C) at 303 K of silver selenide films before and after being annealed, and the errors of these three parameters are ±5%, ±7%, and ±14%, respectively. This figure is related to Figure S5.

silver-rich silver selenide at room temperature (1.8 W/K) (Day et al., 2013) rather than the thermal conductivity of annealed $Ag_{2.3}Se$ pellet, and the thermal conductivity of paper substrate for numerical simulation is 0.8 W/(mK) (Lavrykov and Ramarao, 2012).

Optimal Length of Annealed $Ag_{2.3}Se$ Film by Numerical Simulation

As reported in previous work concerning bulk thermoelectric device, the length of thermoelectric leg plays a key role in determining the output power of thermoelectric generator (Zhang et al., 2018). Generally,

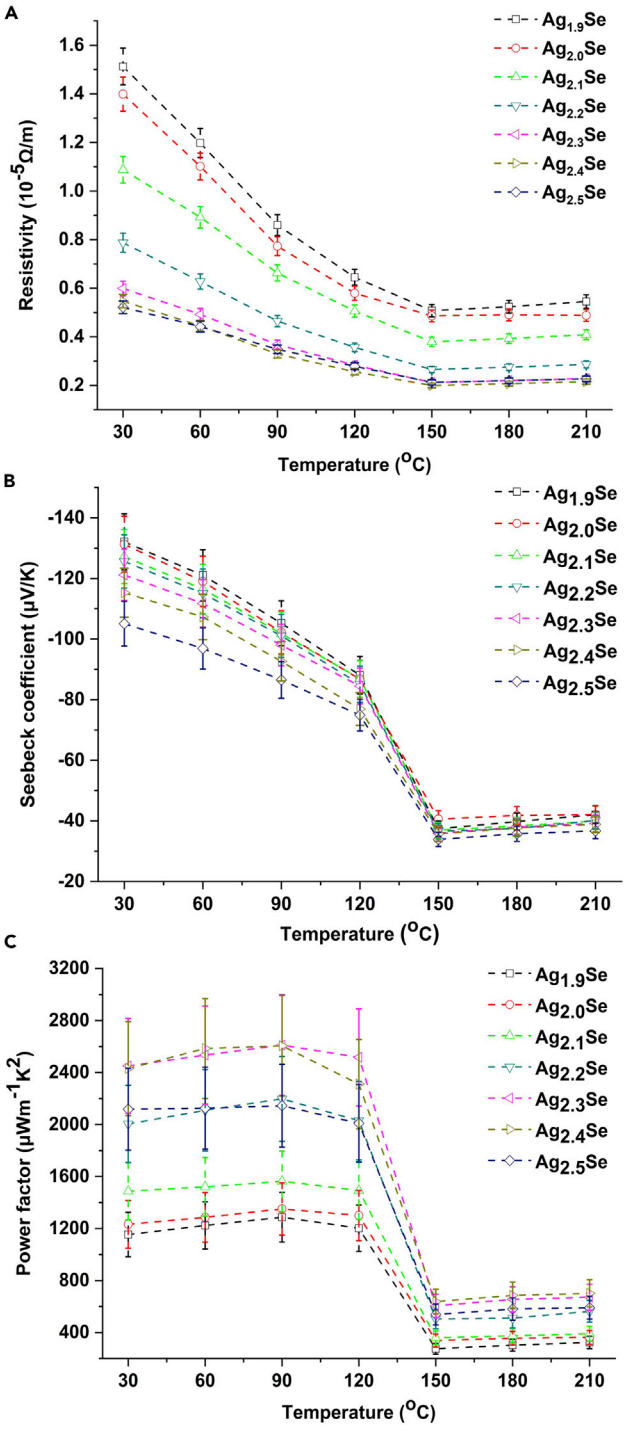

Figure 7. The Thermoelectric Properties of Annealed Silver Selenide Films at Different Temperatures

The electrical resistivities (A), Seebeck coefficients (B), and power factors (C) of annealed silver selenide films at different temperatures, and the errors of these three parameters are ±5%, ±7%, and ±14%, respectively.

reducing the length of thermoelectric film may lead to a too small temperature difference between the two ends of film, and as result, the output voltage of thermoelectric film would be diminished. On the other hand, the electrical resistance of thermoelectric film with excessive length is too large. Most numerical simulations of thermoelectric generators focus on devices based on conventional bulk materials

Sample	Power Factor ($\mu Wm^{-1}K^{-2}$)
Flexible annealed $Ag_{2.3}Se$ film	2451 ± 364 (this work)
5%Te/Ag_2Se bulk materials	1800 (Lim et al., 2019)
$Ag_2Se_{1.06}$ bulk materials	3010 (Mi et al., 2014)
Ag_2Se film on glass substrate	2440 ± 192 (Perez-Taborda et al., 2018)
Flexible nylon-supported Ag_2Se film	987 ± 104 (Ding et al., 2019)
Flexible nylon-supported Cu1Ag4Se3 film	2232 (Lu et al., 2019)
$Bi_2Te_{2.7}Se_{0.3}$ film on glass fiber	2077 (Shin et al., 2017)

Table 2. The Power Factors at Around 300 K of Annealed $Ag_{2.3}Se$ Film in This Work and Representative Thermoelectric Bulk Materials and Flexible Films

(Ferreira-Teixeira and Pereira, 2018; Qiu et al., 2019), and in this work, in order to obtain the ideal output voltage and power of flexible thermoelectric generator fabricated with the annealed $Ag_{2.3}Se$ film, the optimal length of single annealed $Ag_{2.3}Se$ film is investigated through numerical simulation using finite element analysis. As shown in Figure 8, the annealed $Ag_{2.3}Se$ film, silver electrodes, and paper-substrate are simulated to be thin cubes, and aluminum plates are placed on both ends of the film.

Based on the above model, the temperature and potential fields of annealed $Ag_{2.3}Se$ films with different lengths (from 1 mm to 25 mm) are obtained via numerical simulation, and the results are listed in Figure S7. As illustrated in Figure 9, the simulated temperature of cold side (T_c) decreases, whereas the open-circuit voltage (U_{oc}) increases with the ascending length of film and finally reaches a steady state once the length exceeds 13 mm. In the steady state, the temperature difference of hot and cold sides remains nearly unchanged at 25°C and the corresponding theoretic open-circuit voltage is up to about 2.97 mV. This value is a little higher than the experimental result (2.8 mV) due to two possible reasons. First, the actual temperature of hot side of annealed $Ag_{2.3}Se$ film is less than 50°C because of the thermal resistance at the interface between hot side of paper substrate and heating aluminum plate. Second, the actual voltage is measured by contacting probes to electrodes, which inevitably leads to the heat loss at hot side (Jin et al., 2018).

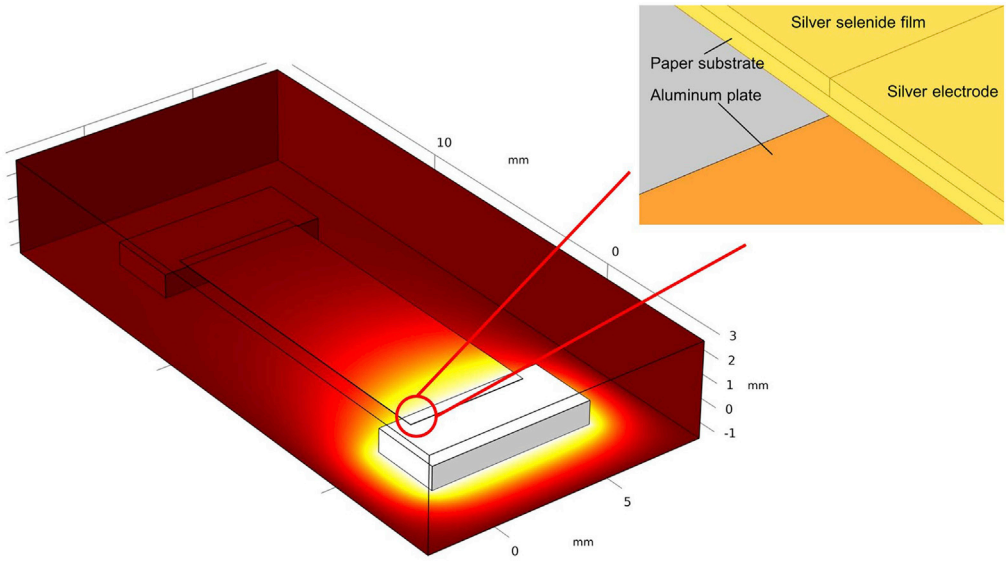

Figure 8. The Three-Dimensional Model of Single Paper-Supported $Ag_{2.3}Se$ Film for Numerical Simulation
This figure is related to Figure S6.

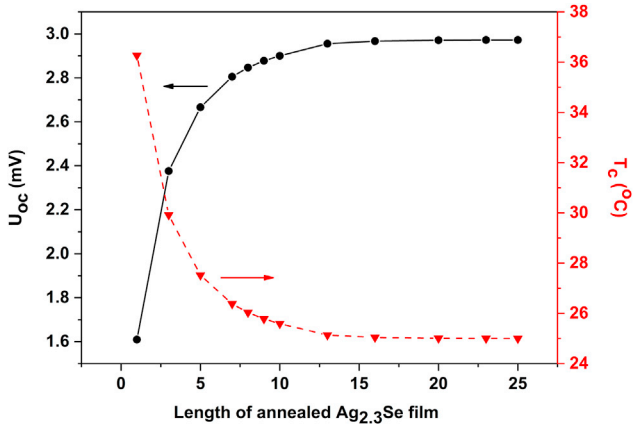

Figure 9. The Simulated Electrical and Thermal Data of Single Annealed $Ag_{2.3}Se$ Film with Different Lengths

The numerically simulated U_{oc} (solid line) and T_c (dash line) of annealed $Ag_{2.3}Se$ films with different lengths. This figure is related to Figure S7.

Thermoelectric Performance of Paper-Supported Silver Selenide Thermoelectric Generator

By series-connecting four pieces of $Ag_{2.3}Se$ films with length of 13 mm, the flexible paper-supported thermoelectric module is fabricated and the photographs of module before and after being annealed are shown in Figure 10A and 10B. The width of each film is 5 mm and the distance between two adjacent films is 3 mm. Figure 10C displays the method for measurement, and the temperatures of hot and cold side are 50°C and 25°C (environmental temperature), respectively. The output voltages and output powers

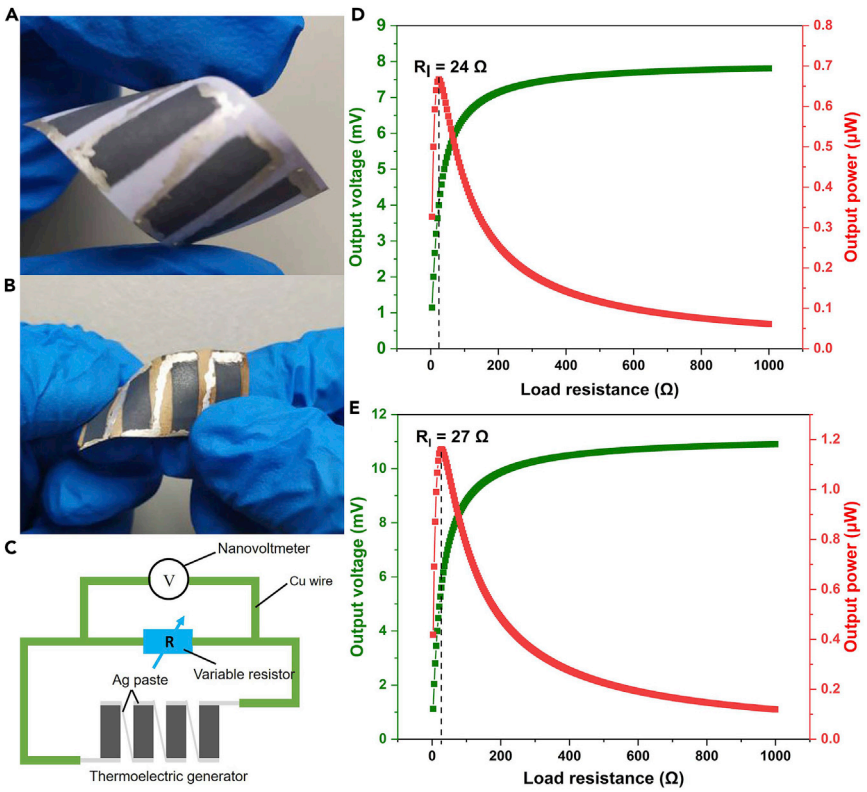

Figure 10. The Actual Thermoelectric Devices and Corresponding Electrical Performance

The photograph of paper-supported $Ag_{2.3}Se$ thermoelectric generator before (A) and after (B) being annealed, the diagram of measuring output voltage of thermoelectric generator (C), and the output voltage and power of thermoelectric generator before (D) and after (E) being annealed at temperature difference of 25 K.

Sample	P_d (W/m^2)	△T (K)	P_d/△T (Wm^{-2}K^{-1})
Annealed $Ag_{2.3}Se$ film (this work)	5.80	25	0.23
Cu1Ag4Se3 film (Lu et al., 2019)	5.42 2.37	45 28	0.12 0.08
C_{60}/TiS_2 nanosheet hybrid film (Wang et al., 2018)	1.68	20	0.08
PANI/SWNT/Te composite film (Wang et al., 2017)	0.62	40	0.02

Table 3. The Output Power Density of Annealed $Ag_{2.3}Se$-Film-Based Device and Previous Representative Film Thermoelectric Devices

of paper-supported $Ag_{2.3}Se$ thermoelectric generator before and after being annealed are shown in Figures 10D and 10E, and the output power is calculated by this formula: $P_l = \frac{U_l^2}{R_l}$, where P_l is the output power, U_l is the voltage across the load variable resistor, namely output voltage, and R_l is the resistance of variable resistor (Madan et al., 2015). As is known to all, The output voltage is calculated by this formula: $U_l = \left(1 - \frac{R_{in}}{R_{in}+R_l}\right) * U_o$, where U_o is the open-circuit voltage of module, R_{in} is the internal resistance of module, and R_l is the load variable resistor. Thus, at a certain temperature difference, the output voltage will increase with the increasing load resistance and eventually infinitely approach the open-circuit voltage. On the other hand, the output power reaches the maximum value when the load resistance equals to the internal resistance of thermoelectric generator.

For the generator before being annealed, the internal resistance measured to be about 24 Ω, and as shown in Figure 10D, the maximum value of output power and the corresponding output voltage are 0.67 μW and 4.05 mV at temperature difference of 25 K. After being annealed, the generator shows a little higher internal resistance of 27 Ω. Figure 10E displays that the maximum value of output power and the corresponding output voltage of annealed generator are improved to be 1.16 μW and 5.60 mV, respectively. Obviously, this improvement of performance is resulted from the enhanced Seebeck coefficient of annealed $Ag_{2.3}Se$ film. The power density of annealed $Ag_{2.3}Se$ module can be calculated by the following equation: $P_d = \frac{P_{max}}{N * S}$, where P_d is the power density, P_{max} is the maximum value of output power, N is number of thermoelectric film, and S is the cross-sectional area of annealed $Ag_{2.3}Se$ film (Lu et al., 2019). And in this work, the N is 4 and the S is calculated by the equation $S = t * w$, where t is the thickness of $Ag_{2.3}Se$ film without substrate (10 μm) and w is the width of $Ag_{2.3}Se$ film (5 mm). Thus, S is 0.05 mm^2 and the P_d is calculated to be

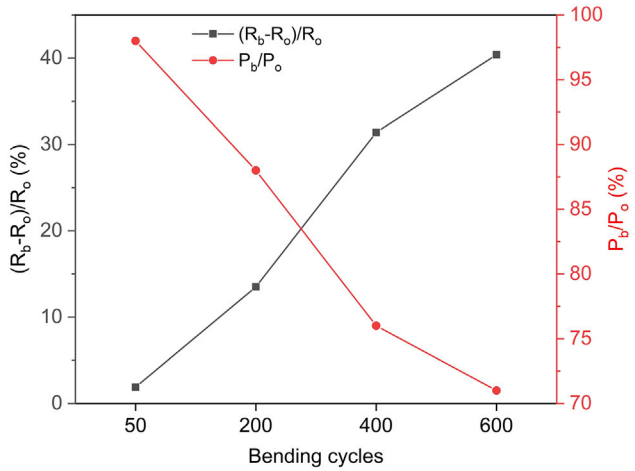

Figure 11. The Internal Resistance and Output Power Ratio as a Function of Bending Cycles

R_o and P_o represent the internal resistance and output power of original device, and R_b and P_b mean the internal resistance and output power of device has been bent for a certain of cycles. This figure is related to Video S1.

Sample	Bending Cycles	$(R_b-R_o)/R_o$
Annealed $Ag_{2.3}Se$ device (this work)	600	40.4%
Ag_2Te NWs film (Gao et al., 2017b)	500	21%
Bi_2Te_3 film (Rojas et al., 2017)	400	140%
Sb_2Te_3 film (Rojas et al., 2017)	400	50%

Table 4. The Comparison of Flexibility Test of Annealed $Ag_{2.3}Se$ Thermoelectric Device and Other Paper-Supported Thermoelectric Films

5.80 W/m^2. As displayed in Table 3, at similar temperature difference, the output power density of annealed $Ag_{2.3}Se$-based module is much higher than that of previous representative film thermoelectric devices, and in the case that temperature difference is 1 K, the output power density of our annealed $Ag_{2.3}Se$ film is also the highest.

The flexibility of annealed $Ag_{2.3}Se$ thermoelectric device has been tested and the result is shown in Figure 11. R_o and P_o represent the internal resistance and output power of original device, and R_b and P_b mean the internal resistance and output power of device has been bent for a certain of cycles. A short video (Video S1) is provided in Supplemental Information to show how we bend the device and the bending radius is about 1 cm. With increasing bending cycles, the internal resistance of device increases while the output power decreases. After 600 bending cycles, the internal resistance of device increases by 40.4% and the output power decreases by 29%. The flexibility test of thermoelectric device has barely been reported in previous articles, thus the result of this flexibility test is compared with that of other single paper-supported thermoelectric film in Table 4. Because the nanowires can form crisscrossed conductive network, the Ag_2Te NWs film, which was reported in our previous work, showed a better flexibility than the annealed $Ag_{2.3}Se$ device. However, due to the tight bond between the $Ag_{2.3}Se$ film and paper substrate, the flexibility of annealed $Ag_{2.3}Se$ device is still superior to the paper-supported Bi_2Te_3 and Sb_2Te_3 films prepared by magnetron sputtering (Rojas et al., 2017).

Limitations of the Study

To improve the output power density of flexible film thermoelectric generator, the length of single thermoelectric film has been optimized by numerical simulation in this work. Although the actual output power density of our generator is superior to that of other flexible film thermoelectric generator, the thermal conductivity of annealed $Ag_{2.3}Se$ film for simulation is a theoretic value rather than an actually measured value because it is difficult to obtain the accurate thermal conductivity of thermoelectric film adhered on a substrate. In further work, we will try our best to obtain the actual thermal conductivity of flexible thermoelectric film for numerical simulation.

METHODS

All methods can be found in the accompanying Transparent Methods supplemental file.

SUPPLEMENTAL INFORMATION

Supplemental Information can be found online at https://doi.org/10.1016/j.isci.2019.100753.

ACKNOWLEDGMENTS

This work was supported by the National Natural Science Foundation of China (Grant No. 51572049, 51772056, 51961011), National Key Research and Development Program of China (No. 2017YFE9128000) and the Natural Science Foundation of Guangxi, China (Grant No. 2018GXNSFAA294135, AD19110020).

AUTHOR CONTRIBUTIONS

J. G. conceived the idea and prepared the nanoparticles, films, and devices. J. G. and S. J. Z. measured the thermoelectric properties of the films and devices. J. G., Y. P., and X. Y. W. characterized the nanoparticles and films. H. J. L and H. F. C. completed the numerical simulation. J. G., L. M., and H. J. L. discussed and analyzed the data. J. G., L. M., H. J. L., and K. K. wrote and edited the manuscript.

DECLARATION OF INTERESTS

The authors declare no competing financial interests.

Received: August 5, 2019
Revised: October 28, 2019
Accepted: November 25, 2019
Published: January 24, 2020

REFERENCES

Bahk, J.-H., Fang, H., Yazawa, K., and Shakouri, A. (2015). Flexible thermoelectric materials and device optimization for wearable energy harvesting. J. Mater. Chem. C *3*, 10362–10374.

Chen, Y., He, M., Liu, B., Bazan, G.C., Zhou, J., and Liang, Z. (2017). Bendable n-type metallic nanocomposites with large thermoelectric power factor. Adv. Mater. *29*, 1604752.

Day, T., Drymiotis, F., Zhang, T., Rhodes, D., Shi, X., Chen, L., and Snyder, G.J. (2013). Evaluating the potential for high thermoelectric efficiency of silver selenide. J. Mater. Chem. C *1*, 7568–7573.

Ding, Y., Qiu, Y., Cai, K., Yao, Q., Chen, S., Chen, L., and He, J. (2019). High performance n-type Ag_2Se film on nylon membrane for flexible thermoelectric power generator. Nat. Commun. *10*, 841.

Du, Y., Xu, J., Paul, B., and Eklund, P. (2018). Flexible thermoelectric materials and devices. Appl. Mater. Today *12*, 366–388.

Dun, C., Hewitt, C.A., Huang, H., Xu, J., Zhou, C., Huang, W., Cui, Y., Zhou, W., Jiang, Q., and Carroll, D.L. (2015). Flexible n-type thermoelectric films based on Cu-doped Bi2Se3 nanoplate and Polyvinylidene Fluoride composite with decoupled Seebeck coefficient and electrical conductivity. Nano Energy *18*, 306–314.

Ferhat, M., and Nagao, J. (2000). Thermoelectric and transport properties of β-Ag_2Se compounds. J. Appl. Phys. *88*, 813–816.

Ferreira-Teixeira, S., and Pereira, A.M. (2018). Geometrical optimization of a thermoelectric device: numerical simulations. Energy Convers. Manag. *169*, 217–227.

Gao, J., Liu, C., Miao, L., Wang, X., Peng, Y., and Chen, Y. (2016). Enhanced power factor in flexible reduced graphene oxide/nanowires hybrid films for thermoelectrics. RSC Adv. *6*, 31580–31587.

Gao, M., Li, L., and Song, Y. (2017a). Inkjet printing wearable electronic devices. J. Mater. Chem. C *5*, 2971–2993.

Gao, J., Miao, L., Liu, C., Wang, X., Peng, Y., Wei, X., Zhou, J., Chen, Y., Hashimoto, R., Asaka, T., and Koumoto, K. (2017b). A novel glass-fiber-aided cold-press method for fabrication of n-type Ag_2Te nanowires thermoelectric film on flexible copy-paper substrate. J. Mater. Chem. A *5*, 24740–24748.

Ge, Z.-H., Zhao, L.-D., Wu, D., Liu, X., Zhang, B.-P., Li, J.-F., and He, J. (2016). Low-cost, abundant binary sulfides as promising thermoelectric materials. Mater. Today *19*, 227–239.

Hu, X., Li, F., and Song, Y. (2019). Wearable power source: a newfangled feasibility for perovskite photovoltaics. ACS Energy Lett. *4*, 1065–1072.

Jeon, T., Jin, H.M., Lee, S.H., Lee, J.M., Park, H.I., Kim, M.K., Lee, K.J., Shin, B., and Kim, S.O. (2016). Laser crystallization of organic–inorganic hybrid perovskite solar cells. ACS Nano *10*, 7907–7914.

Jin, W., Liu, L., Yang, T., Shen, H., Zhu, J., Xu, W., Li, S., Li, Q., Chi, L., Di, C.-a., and Zhu, D. (2018). Exploring Peltier effect in organic thermoelectric films. Nat. Commun. *9*, 3586.

Kim, S.J., Lee, H.E., Choi, H., Kim, Y., We, J.H., Shin, J.S., Lee, K.J., and Cho, B.J. (2016). High-performance flexible thermoelectric power generator using laser multiscanning lift-off process. ACS Nano *10*, 10851–10857.

Kroon, R., Mengistie, D.A., Kiefer, D., Hynynen, J., Ryan, J.D., Yu, L., and Müller, C. (2016). Thermoelectric plastics: from design to synthesis, processing and structure–property relationships. Chem. Soc. Rev. *45*, 6147–6164.

Lavrykov, S.A., and Ramarao, B.V. (2012). Thermal properties of copy paper sheets. Drying Technol. *30*, 297–311.

Lee, C., Park, Y.-H., and Hashimoto, H. (2007). Effect of nonstoichiometry on the thermoelectric properties of a Ag_2Se alloy prepared by a mechanical alloying process. J. App. Phys. *101*, 024920.

Li, W., Lin, S., Ge, B., Yang, J., Zhang, W., and Pei, Y. (2016). Low sound velocity contributing to the high thermoelectric performance of Ag_8SnSe_6. Adv. Sci. *3*, 1600196.

Lim, K.H., Wong, K.W., Liu, Y., Zhang, Y., Cadavid, D., Cabot, A., and Ng, K.M. (2019). Critical role of nanoinclusions in silver selenide nanocomposites as a promising room temperature thermoelectric material. J. Mater. Chem. C *7*, 2646–2652.

Liu, J., Wang, X., Li, D., Coates, N.E., Segalman, R.A., and Cahill, D.G. (2015). Thermal conductivity and elastic constants of PEDOT: PSS with high electrical conductivity. Macromolecules *48*, 585–591.

Lou, Z., Li, L., Wang, L., and Shen, G. (2017). Recent progress of self-powered sensing systems for wearable electronics. Small *13*, 1701791.

Lu, Y., Qiu, Y., Cai, K., Ding, Y., Wang, M., Jiang, C., Yao, Q., Huang, C., Chen, L., and He, J. (2019). Ultrahigh power factor and flexible silver selenide-based composite film for thermoelectric devices. Energ. Environ. Sci. https://doi.org/10.1039/C1039EE01609K.

Madan, D., Wang, Z., Wright, P.K., and Evans, J.W. (2015). Printed flexible thermoelectric generators for use on low levels of waste heat. Appl. Energ. *156*, 587–592.

Mi, W., Qiu, P., Zhang, T., Lv, Y., Shi, X., and Chen, L. (2014). Thermoelectric transport of Se-rich Ag_2Se in normal phases and phase transitions. Appl. Phys. Lett. *104*, 133903.

Perez-Taborda, J.A., Caballero-Calero, O., Vera-Londono, L., Briones, F., and Martin-Gonzalez, M. (2018). High thermoelectric zT in n-type silver selenide films at room temperature. Adv. Energy Mater. *8*, 1702024.

Qiu, P., Mao, T., Huang, Z., Xia, X., Liao, J., Agne, M.T., Gu, M., Zhang, Q., Ren, D., Bai, S., et al. (2019). High-efficiency and stable thermoelectric module based on liquid-like materials. Joule *3*, 1538–1548.

Rojas, J.P., Conchouso, D., Arevalo, A., Singh, D., Foulds, I.G., and Hussain, M.M. (2017). Paper-based origami flexible and foldable thermoelectric nanogenerator. Nano Energy *31*, 296–301.

Shin, S., Kumar, R., Roh, J.W., Ko, D.-S., Kim, H.-S., Kim, S.I., Yin, L., Schlossberg, S.M., Cui, S., You, J.-M., et al. (2017). High-performance screen-printed thermoelectric films on fabrics. Sci. Rep. *7*, 7317.

Wang, L., Yao, Q., Shi, W., Qu, S., and Chen, L. (2017). Engineering carrier scattering at the interfaces in polyaniline based nanocomposites for high thermoelectric performances. Mater. Chem. Front. *1*, 741–748.

Wang, L., Zhang, Z., Geng, L., Yuan, T., Liu, Y., Guo, J., Fang, L., Qiu, J., and Wang, S. (2018). Solution-printable fullerene/TiS_2 organic/inorganic hybrids for high-performance flexible n-type thermoelectrics. Energy Environ. Sci. *11*, 1307–1317.

Weathers, A., Khan, Z.U., Brooke, R., Evans, D., Pettes, M.T., Andreasen, J.W., Crispin, X., and Shi, L. (2015). Significant electronic thermal transport in the conducting polymer poly(3,4-ethylenedioxythiophene). Adv. Mater. *27*, 2101–2106.

Xiao, C., Xu, J., Li, K., Feng, J., Yang, J., and Xie, Y. (2012). Superionic phase transition in silver chalcogenide nanocrystals realizing optimized thermoelectric performance. J. Am. Chem. Soc. *134*, 4287–4293.

Yang, H., Leow, W.R., and Chen, X. (2018). 3D printing of flexible electronic devices. Small Methods *2*, 1700259.

Zhang, A.B., Wang, B.L., Pang, D.D., Chen, J.B., Wang, J., and Du, J.K. (2018). Influence of leg geometry configuration and contact resistance on the performance of annular thermoelectric generators. Energy Convers. Manag. *166*, 337–342.

Zhao, L.-D., Lo, S.-H., Zhang, Y., Sun, H., Tan, G., Uher, C., Wolverton, C., Dravid, V.P., and Kanatzidis, M.G. (2014). Ultralow thermal conductivity and high thermoelectric figure of merit in SnSe crystals. Nature *508*, 373.

Zi, Y., and Wang, Z.L. (2017). Nanogenerators: an emerging technology towards nanoenergy. APL Mater. *5*, 074103.

ISCI, Volume *23*

Supplemental Information

Thermoelectric Flexible Silver Selenide Films: Compositional and Length Optimization

Jie Gao, Lei Miao, Huajun Lai, Sijing Zhu, Ying Peng, Xiaoyang Wang, Kunihito Koumoto, and Huanfu Cai

Supplemental Information

This PDF file includes:

Transparent Methods

Figure S1 to S7

Table S1

Video S1

Transparent Methods

EXPERIMENTAL PROCEDURES

Materials

Silver nitrate ($AgNO_3$, 99.8%) , selenium powder (Se, 99.9%), ethylenediamine ($C_2H_8N_2$, 99%) and polyvinylpyrrolidone (PVP, M.W. 58000) were purchased from Aladdin Chemical Co., Ltd. Ethylene glycol ($C_2H_6O_2$, 99%) was bought from Sinopharm Chemical Reagent Co., Ltd. The glass fiber membrane was obtained from Yuyan (Shanghai) Chemical Co. and the copy-paper was produced by Onhing (Shanghai) Paper Co., Ltd. All of these materials were used without further purification.

Preparation of silver selenide NPs dispersion

First, a certain amount of Se powder and 10 mg PVP were dissolved in 15 mL ethylenediamine under vigorous magnetic stirring at room temperature for 30 min. Then, under ultra-sonication, some $AgNO_3$ was dissolved in 5 mL ethylenediamine at room temperature. Subsequently, the $AgNO_3$ solution was quickly poured in the Se solution and the mixture was transferred into a 25 mL Teflon-lined stainless steel autoclave. The autoclave was sealed and maintained at 180 ^oC for 5 h. After the autoclave was cooled to room temperature naturally, black precipitate was collected by centrifugation and washed with ethanol for two times. Finally, the product was dispersed in 10 mL of ethylene glycol to form a uniform black dispersion. The total amount of the $AgNO_3$ and Se powder for all samples is 0.4187 g and molar ratio of $AgNO_3$ and Se varies from 1.9 to 2.5.

Fabrication of paper-supporting silver selenide NPs films

First, with the aid of vacuum filtration, 12 drops (the volume of 28 drops is about 1 mL) of silver selenide NPs dispersion were drop-cast on a piece of glass-fiber sheet with size of 20 mm × 5 mm. Then after the glass-fiber sheet coated with silver selenide NPs was dried in dynamic vacuum at 80 ^{o}C for 4 h, it was sandwiched between 2 pieces of copy-paper and pressed at 40 MPa for 30 s. Afterwards the debris of glass-fiber was removed and the paper-supporting silver selenide NPs film was obtained. Finally, in the flowing Ar/H_2 atmosphere, the paper-supporting films were annealed in a tube furnace at 250 ^{o}C for 2 h. The samples were named as $Ag_{1.9}Se$, $Ag_{2.0}Se$, $Ag_{2.1}Se$, $Ag_{2.2}Se$ $Ag_{2.3}Se$, $Ag_{2.4}Se$ and $Ag_{2.5}Se$, however, it should be noted that the actual molar ratios of Ag/Se in the samples do not equal to the corresponding molar ratios of $AgNO_3$ to Se powder.

Characterization

The crystallographic structure of silver selenide films were studied by X-ray diffractometer (XRD) using Cu Ka radiation (Bruker, D8 Advance). The size and morphology of silver selenide nanoparticles and films were revealed by scanning electron microscopy (SEM), operated on a Hitachi S-4800 FESEM microscope and transmission electron microscopy (TEM), performed on a Thermo Fisher Talos F200X microscope. The composition of silver selenide films were analyzed by energy-dispersive X-ray spectroscopy (EDS) using the Oxford energy dispersive X-ray detectors attached with the microscopes. Electrical conductivities and Seebeck coefficients of silver selenide films were taken via a Seebeck coeffcient/electrical resistivity measuring system (Ulvac-Riko, ZEM-3) in argon (99.999%) atmosphere

with temperature gradients of 20, 30 and 40 ^{o}C. Charge carrier mobility and carrier concentration of silver selenide films were obtained by measuring the Hall effect (Toyo, Resitest 8300). The thermal diffusivity was measured via a laser flash diffusivity apparatus (NETZSCH LFA 467). The specific heat capacity was obtained using a differential scanning calorimeter (NETZSCH 404 F3). The resistances of silver selenide films and generators were measured by a multimeter (Fluke, 12E+). Output voltages of paper-supporting generators were collected by a nanovoltmeter (Keithley, 2182A).

Numerical simulation

By finite element modeling, the optimal length of single annealed $Ag_{2.3}Se$ film is numerically simulated through COMSOL Multiphysics 5.4a software. The size of $Ag_{2.3}Se$ film is set as L mm × 5 mm × 10 μm (L is variable), the electrodes are set as 0.5 mm × 5 mm × 10 μm and the paper substrate is set as (L+1) mm × 5mm × 30 μm. The size of aluminum plates is set as 7 mm × 3 mm × 1 mm and the hot side and cold side of aluminum plates are set as 50 ^{o}C and 25 ^{o}C (environmental temperature), respectively. The size of air domain is set as 12 mm × (L+2) mm × 4mm. In the whole model, at the interfaces among the annealed $Ag_{2.3}Se$ film, electrodes, paper substrate and aluminum plates, the contact thermal and electrical resistance are ignored. The thermal conductivities of paper-substrate and annealed $Ag_{2.3}Se$ film are set as 0.8 W/(mK) and 1.8 W/(mK), respectively, and the heat is dissipated from the whole model to atmosphere by natural convection.

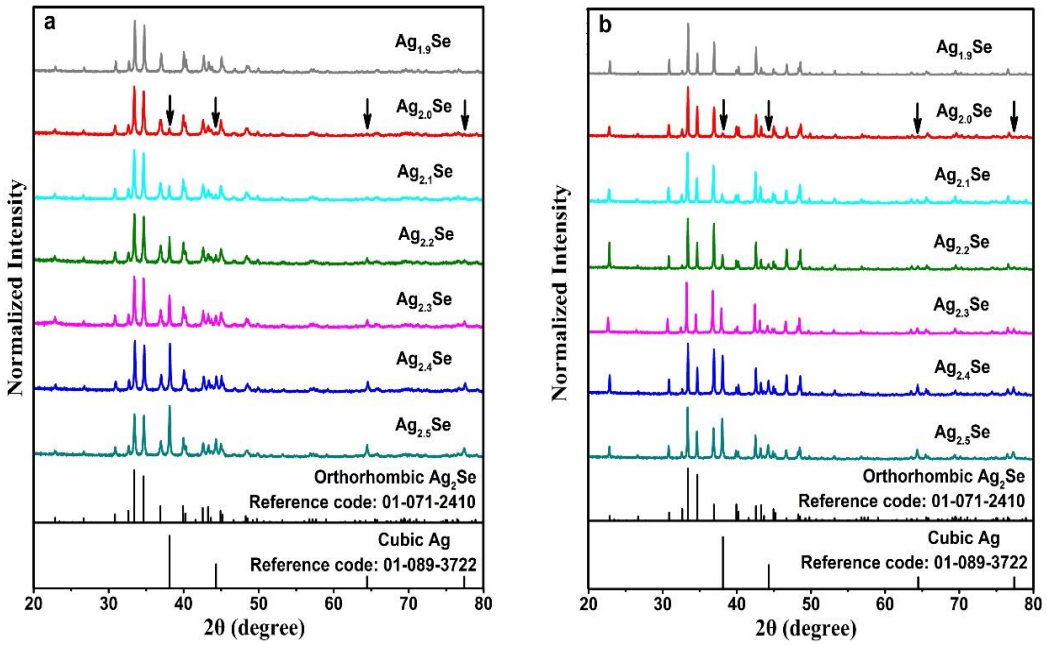

Figure S1. The XRD spectra of all silver selenide films before (a) and after (b) being annealed, related to Figure 1.

As displayed in Figure S1, all peaks in the XRD spectra of $Ag_{1.9}Se$ film can be indexed to the orthorhombic Ag_2Se and the XRD spectra of other films show characteristic peaks of orthorhombic Ag_2Se and cubic Ag. By comparing Figure S1a with Figure S1b, the annealing treatment leads to the weakened intensity of characteristic peaks of Ag and enhanced intensity of some characteristic peaks of Ag_2Se.

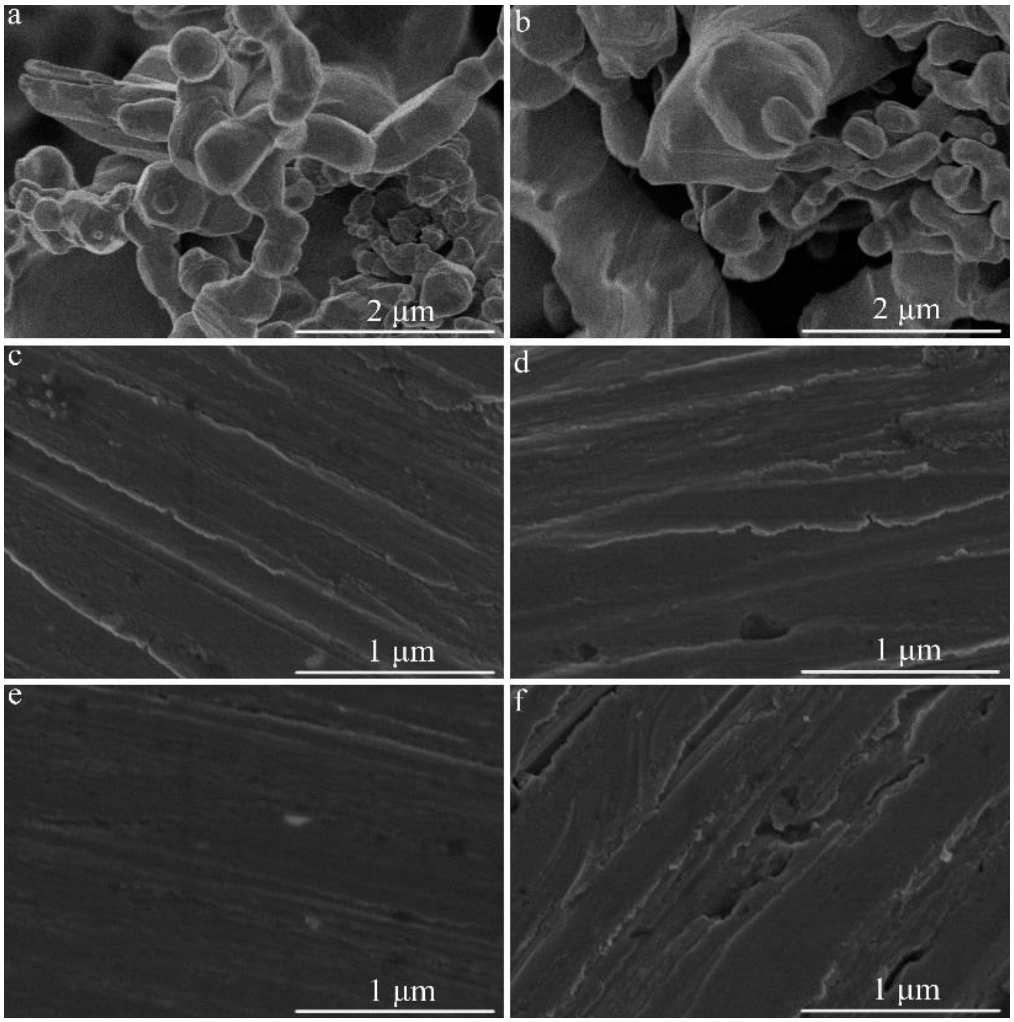

Figure S2. The representative SEM images of silver selenide particles and paper-supporting films. $Ag_{2.1}Se$ and $Ag_{2.3}Se$ particles (a and b), $Ag_{2.1}Se$ and $Ag_{2.3}Se$ films (c and d) and annealed $Ag_{2.1}Se$ and $Ag_{2.3}Se$ films (e and f), related to Figure 3.

Figure S2 reveals the morphology of $Ag_{2.1}Se$ and $Ag_{2.3}Se$ particles and films. As shown in Figure S2a and Figure S2b, the large-sized and small-sized particles with irregular shape can also be found in these two samples. It can be observed from Figure S2c to Figure S2f that the surface morphology of silver selenide films are similar and the annealing treatment has little impact on the morphology of silver selenide films.

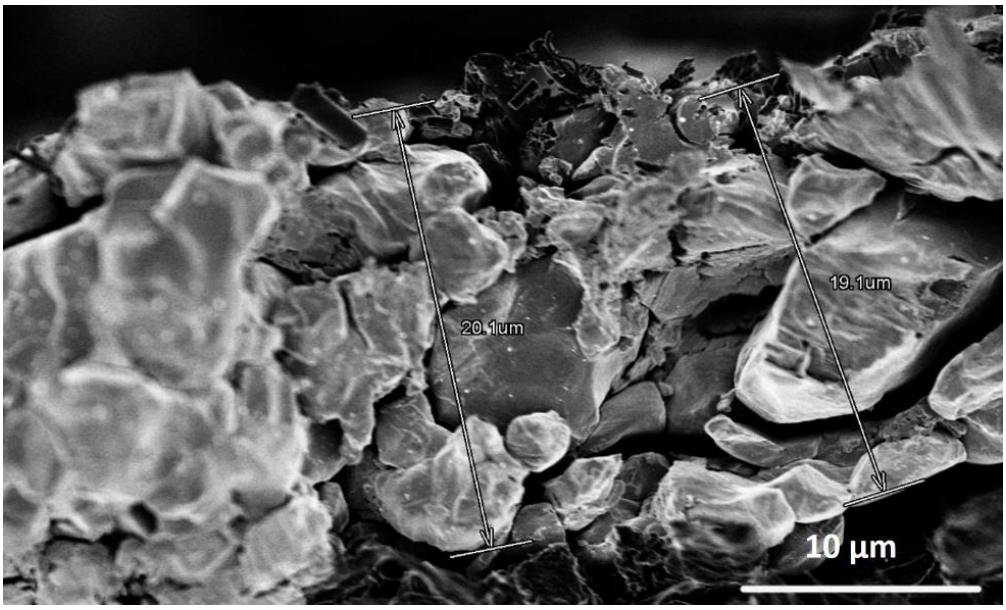

Figure S3. The cross-sectional SEM image of annealed $Ag_{2.5}Se$ film prepared using 25 drops of dispersion, related to Figure 3.

To measure the thickness of the silver selenide film accurately, a piece of annealed $Ag_{2.5}Se$ film is prepared using 25 drops of dispersion, and the cross-sectional SEM image of this film is shown in Figure S3. From this figure, the thickness of this film is about 20 μm, thus the thickness of films prepared with 12 drops of dispersion is about 10 μm.

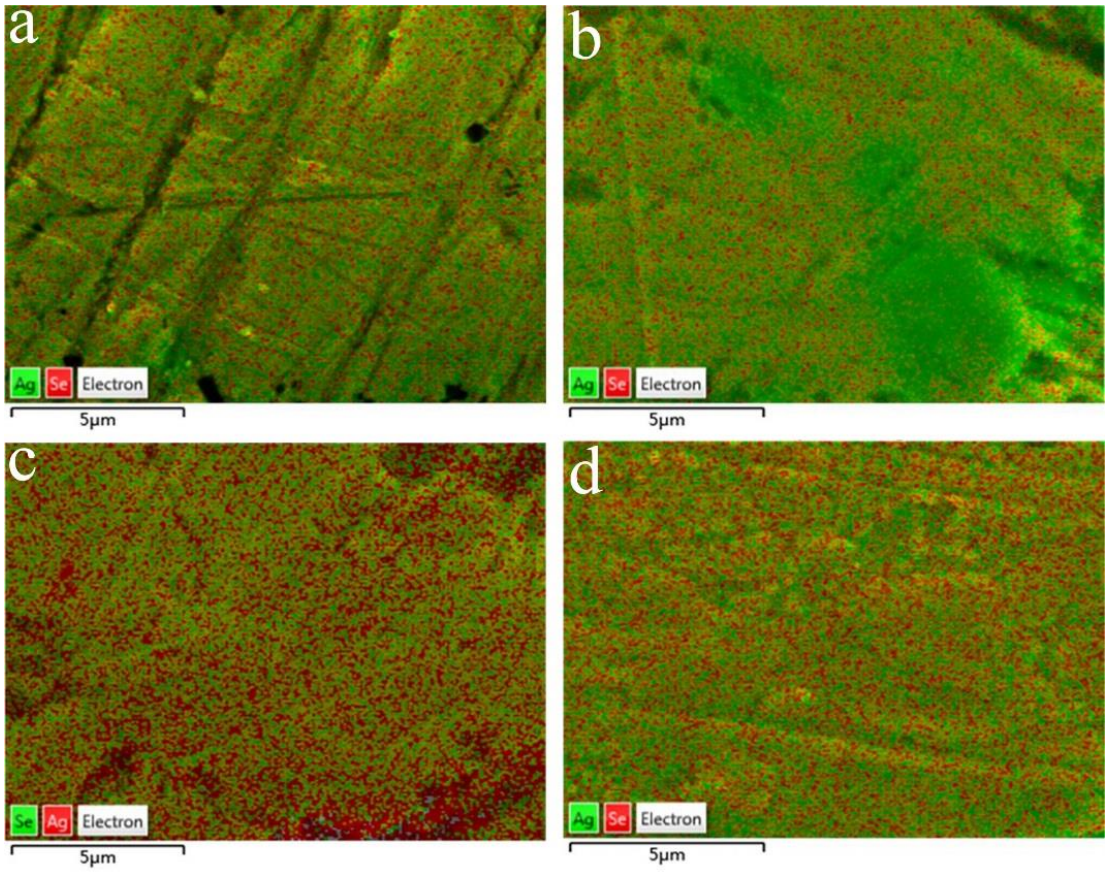

Figure S4. The representative SEM-EDS maps of silver selenide films before and after being annealed. $Ag_{2.1}Se$ film (a), $Ag_{2.3}Se$ film (b), annealed $Ag_{2.1}Se$ film (c) and $Ag_{2.3}Se$ film (d), related to Figure 4 and Table 1.

As shown in Figure S4, compared with the SEM-EDS maps of $Ag_{2.1}Se$ and $Ag_{2.3}Se$ films before being annealed, the signal of Ag element in SEM-EDS maps of corresponding annealed films is obviously reduced and the area of Ag aggregations in annealed $Ag_{2.3}Se$ films is also remarkably diminished.

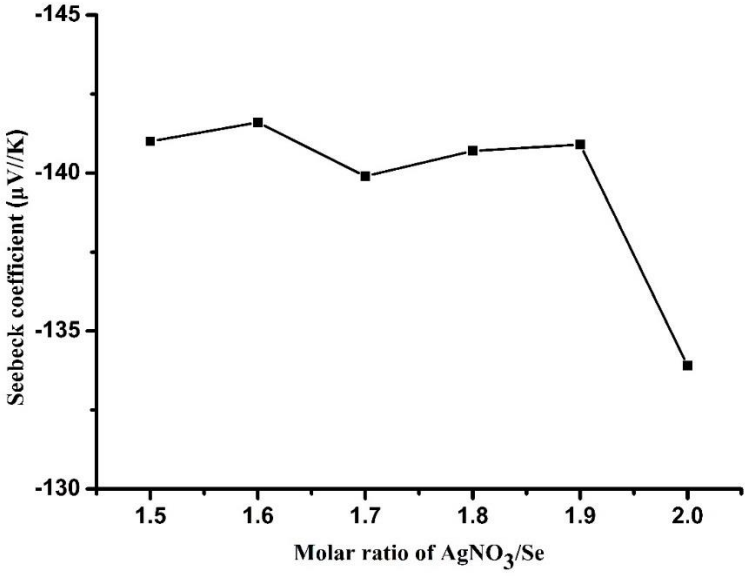

Figure S5. The Seebeck coefficient at 303 K of silver selenide films (from $Ag_{1.5}Se$ to $Ag_{2.0}Se$) before being annealed, related to Figure 6.

The Seebeck coefficients of films prepared with smaller ratios of $AgNO_3$/Se (from 1.8 to 1.5) are displayed in Figure S5. It can be concluded from this figure that the further reduction of $AgNO_3$ is not helpful to improve the Seebeck coefficient of silver selenide film.

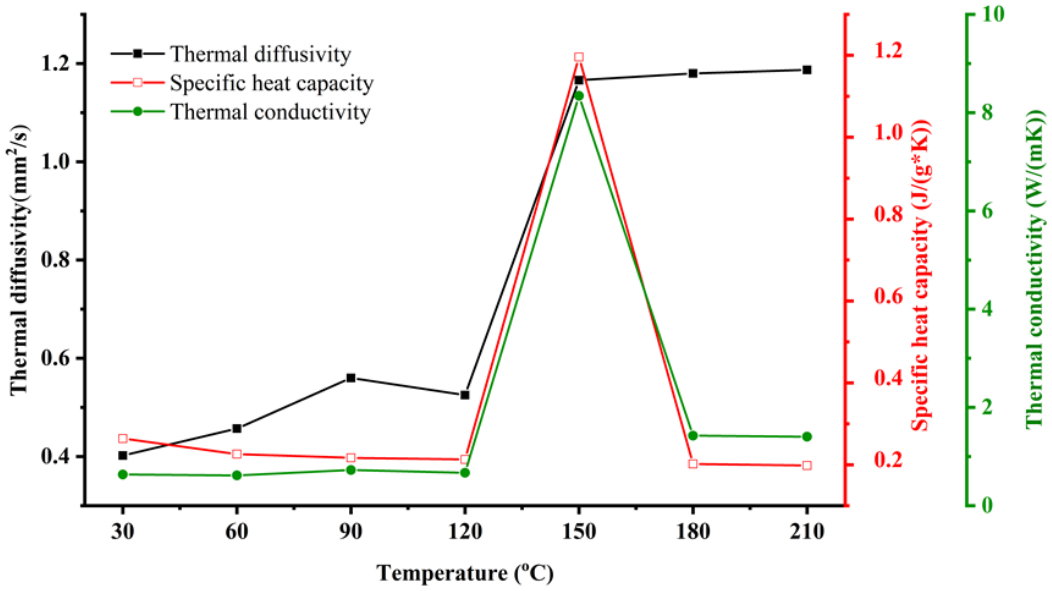

Figure S6. The temperature dependent thermal diffusivity, specific heat capacity and thermal conductivity of annealed $Ag_{2.3}Se$ pellet, related to Figure 8.

In this figure, the thermal conductivity κ is calculated as $\kappa = \alpha * C_p * \rho$, where α is thermal diffusivity, C_p is specific heat capacity and ρ is density of pellet (5.981 g/cm3). As shown in this figure, the thermal conductivity of annealed $Ag_{2.3}Se$ sample at 30 °C is 0.635 W/(mK), and if the ZT value was calculated using this thermal conductivity and PF value of annealed $Ag_{2.3}Se$ film, an ultra-high ZT of 1.12 at 30°C would be obtained. We think that this thermal conductivity is credible but it probably cannot be applied for annealed $Ag_{2.3}Se$ film since the electrical property and thermal conductivity of pellet and film seem to be different due to the influence of substrate. Thus, the theoretic thermal conductivity of silver-rich silver selenide at room temperature of 1.8 W/K is used as the thermal conductivity for our annealed $Ag_{2.3}Se$ film

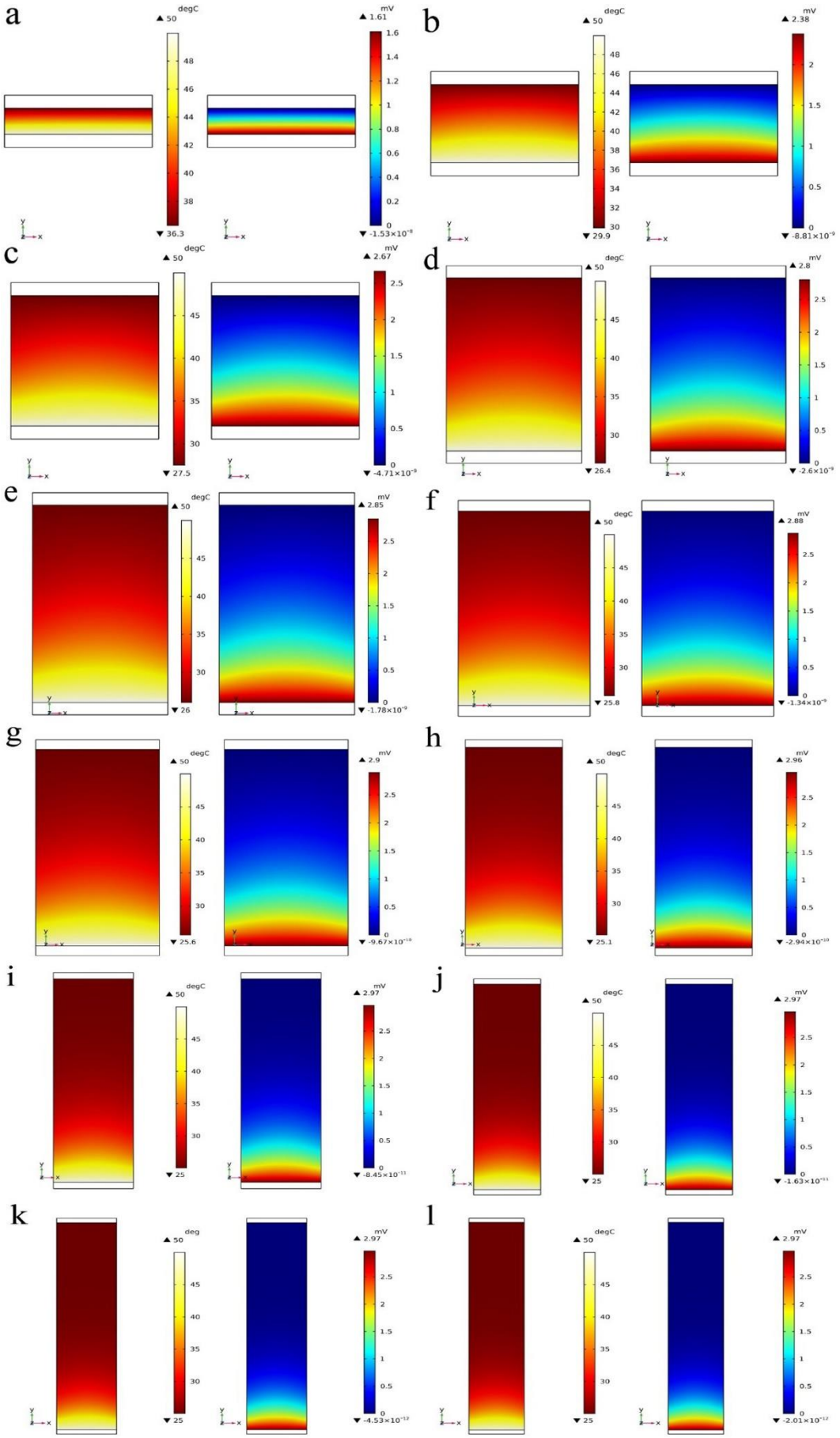
a
degC
▲ 50
48
46
44
42
40
38
▼ 36.3
mV
▲ 1.61
1.6
1.4
1.2
1
0.8
0.6
0.4
0.2
0
▼ -1.53×10⁻⁸
b
degC
▲ 50
48
46
44
42
40
38
36
34
32
30
▼ 29.9
mV
▲ 2.38
2
1.5
1
0.5
0
▼ -8.81×10⁻⁹
c
degC
▲ 50
45
40
35
30
▼ 27.5
mV
▲ 2.67
2.5
2
1.5
1
0.5
0
▼ -4.71×10⁻⁹
d
degC
▲ 50
45
40
35
30
▼ 26.4
mV
▲ 2.8
2.5
2
1.5
1
0.5
0
▼ -2.6×10⁻⁹
e
degC
▲ 50
45
40
35
30
▼ 26
mV
▲ 2.85
2.5
2
1.5
1
0.5
0
▼ -1.78×10⁻⁹
f
degC
▲ 50
45
40
35
30
▼ 25.8
mV
▲ 2.88
2.5
2
1.5
1
0.5
0
▼ -1.34×10⁻⁹
g
degC
▲ 50
45
40
35
30
▼ 25.6
mV
▲ 2.9
2.5
2
1.5
1
0.5
0
▼ -9.67×10⁻¹⁰
h
degC
▲ 50
45
40
35
30
▼ 25.1
mV
▲ 2.96
2.5
2
1.5
1
0.5
0
▼ -2.94×10⁻¹⁰
i
degC
▲ 50
45
40
35
30
▼ 25
mV
▲ 2.97
2.5
2
1.5
1
0.5
0
▼ -8.45×10⁻¹¹
j
degC
▲ 50
45
40
35
30
▼ 25
mV
▲ 2.97
2.5
2
1.5
1
0.5
0
▼ -1.63×10⁻¹¹
k
deg
▲ 50
45
40
35
30
▼ 25
mV
▲ 2.97
2.5
2
1.5
1
0.5
0
▼ -4.53×10⁻¹²
l
degC
▲ 50
45
40
35
30
▼ 25
mV
▲ 2.97
2.5
2
1.5
1
0.5
0
▼ -2.01×10⁻¹²

Figure S7. The numerically simulated temperature and potential fields of annealed $Ag_{2.3}Se$ films with different lengths. 1 mm (a), 3 mm (b), 5 mm (c), 7 mm (d), 8 mm (e), 9 mm (f), 10 mm (g), 13 mm (h), 16 mm (i), 20 mm (j), 23 mm (k) and 25 mm (l), related to Figure 9.

The temperature and potential fields of annealed $Ag_{2.3}Se$ films with different lengths (from 1 mm to 25 mm) are obtained via numerical simulation, and the results are listed in Figure S7. Notably, due to the changing aspect ratio, the width of simulated films looks different, but actually they are all 5 mm. It can be concluded from the temperature and potential fields that the temperature difference and open-circuit voltage (U_{oc}) increase with the ascending length of film and finally reach a steady state once the length exceeds 13 mm.

Table S1. The full width at half maximum (FWHM) values of (112) plane for all films before and after being annealed, related to Figure 1.

	FWHM of (112) plane (before annealing)	FWHM of (112) plane (after annealing)
$Ag_{1.9}Se$	0.164	0.098
$Ag_{2.0}Se$	0.198	0.144
$Ag_{2.1}Se$	0.209	0.148
$Ag_{2.2}Se$	0.192	0.106
$Ag_{2.3}Se$	0.196	0.116
$Ag_{2.4}Se$	0.191	0.097
$Ag_{2.5}Se$	0.208	0.136

As displayed in Table S1, for all annealed silver selenide films, the full width at half maximum (FWHM) values of dominant peak ((112) plane) are reduced, implying that the annealing treatment leads to the enhanced crystallinity of Ag_2Se phase.

Video S1. The video about bending cycles of annealed $Ag_{2.3}Se$ thermoelectric device, related to Figure 11.

It can be observed from this video that the bending radius is about 1 cm.